

3D - A new generation imaging spectrometer

A. Krabbe, L. Weitzel, H. Kroker, L.E. Tacconi-Garman, M. Cameron,
N. Thatte, G. Sämann, T. Böker, R. Genzel and S. Drapatz

All authors: Max-Planck Institut für Extraterrestrische Physik (MPE)
Postbox 1603
D-85740 Garching, Germany

ABSTRACT

3D, the next generation near-IR spectrometer developed at the MPE, offers, in a single integration, the opportunity to image an 8"×8" field with a pixel scale of 0.5" or 0.3" across the entire K- or H-band simultaneously at a spectral resolution of R=1000 or R=2000 (K). Combining the advantages of imaging and spectroscopy increases the observing efficiency on small extended objects (e.g. galactic nuclei) by such a large factor over existing grating or Fabry-Perot spectrometers that subarcsecond near-IR spectroscopy on faint Seyferts, starbursts, quasars or distant galaxies clusters becomes feasible for the first time on 4m class telescopes. 3D, including a NICMOS III FPA at 25 e⁻/single read, has been successfully operated at telescopes such as the 4.2m WHT, 3.5m Calar Alto and 2.2m La Silla. An additional tip-tilt seeing corrector for 3D called **ROGUE** correcting on up to 18th mag stars at 4m-class-telescopes was successfully commissioned in Summer 94. The optical and electronic design of 3D as well as recent results are presented.

Keywords: NIR, Spectrometer, Imaging, Grism, Slicer, Datacube, Galaxies

1. INTRODUCTION

The technique of imaging spectroscopy in the near-infrared (NIR, 1.2 - 2.45 μm) on subarcsec scale is only a few years old, but has already proven its potential of making fundamental impacts on various extragalactic astrophysical issues. The term "imaging spectroscopy" means that at every position in a field a spectrum has been obtained. The information content is then equivalent to a 3 dimensional datacube which comprises the spatial information about the observed object in two dimension whereas the spectral information lies in the third dimension.

Two techniques have mainly been applied so far: Stepping the long slit of a (grating) spectrometer across the object and scanning a Fabry-Perot interferometer (FPI) through the wavelengths while staring at the object. Both methods work well at spatial resolutions $\geq 1''$ and have shown great results if the objects are bright (Blietz et al. 1994; Krabbe et. al. 1991; Krabbe et al. 1993; Lutz et al. 1993). However many of today's exciting targets tend to be small and relatively faint and if such extended objects (e.g. nuclei of galaxies or high z galaxies) are to be observed on subarcsec scale both techniques have a few of disadvantages:

- Both methods can only acquire two of the three dimensions of the data cube at a time. The third dimension has to be obtained sequentially: In the slit spectrometer it is the second spatial dimension, in the case of the FPI it is the dimension of wavelength. This sequential stepping takes a long time and is very inefficient if high spatial resolution and/or good spectral resolution is desired. Assume an object of only 10" diameter emitting broad lines that 1000 km/s FWHM (e.g. AGN) has to be observed with a spatial sampling of 0.5" and spectral resolution of 300 km/s. In case of the slit spectrometer 20 slit positions, in case of a FPI between 5 and 20 wavelength positions per line have to be integrated on in order to complete the observation. If a single integration requires more than about 1000 secs of integration time, both methods may not be applicable any more.
- Both methods add systematic noise to the data. Even bright targets often require some hours of observing time in order to complete the task. During the integration, atmospheric conditions constantly change and thus influence the quality of the data. The fact that spatially or spectrally related data have to be obtained sequentially now turns into a real handicap: Variations of seeing, airmass and OH emission lines as they typically occur during the night as well as imperfect telescope pointing reproducibility will affect different sets of data differently and can make the construction of a homogeneous data cube more difficult if sometimes not impossible. The data of a slit spectrometer are mostly affected by slit position uncertainties and seeing variations, in case of a FPI seeing variations and changes in atmospheric transmission predominate. The combined effect of the contribution mentioned is an increase in the noise level of the spectra and images by a factor of between 3 and 5. Sometimes a solution could

be to use shorter single integration times and repeat the observing sequence several times. However the result may then be dominated by detector read-noise instead of photon background noise.

- Both methods do not make effective use of the field of view (FOV) provided by the instruments. The slit length of NIR long slit spectrometers is typically of the order of 3 arcmin. If the object diameter is 10", only 11% of the slit area is effectively used, even if one includes a factor of 2 to account for the fact that sky spectra are required to subtract the background from the on-source measurement. In the case of a FPI the situation is similar: If small objects are being observed a large fraction of the FOV is filled with sky background, most of which is wasted.

Summarising these arguments, an instrument capable of obtaining a complete data cube in a single integration and at the same time avoiding the contribution of atmospheric noise could easily cut down on the integration time by a factor of between 10 and 30 or more compared to conventional instruments, depending on the morphology and the number of interesting NIR spectral lines emitted by the specific object. In addition such an instrument offers two additional advantages that should not be overlooked:

- It delivers reliable and consistent data under less favourable weather conditions, especially if shorter periods of good weather prevail.
- The requirements for positioning a source are greatly reduced compared to a slit spectrometer. There is no need to exactly place the object on the slit because the FOV is covered with multiple slits. Faint objects only have to be positioned within the FOV which is much easier and often saves the effort especially if the position or the morphology is not known exactly.

Such an instrument, called 3D, has been developed at the MPE and has been deployed very successfully at a number of 2 to 4m-class-telescopes such as the 4.2 m WHT, La Palma, 3.5 m Calar Alto, and 2.2 m ESO, Chile (Weitzel 1994). In the following paper the working principle and design of 3D is presented together with results that have been obtained recently. A brief introduction into the data reduction procedure has also been added because the data are somewhat more complex in structure compared to conventional instruments.

2. Design of the Instrument

2.1 The working principle

The task to image a three dimensional data cube on a two dimensional detector requires a transformation of three dimensions into two. Therefore the main constituent of the 3D instrument is an image slicer working at ambient temperature, which transforms a two dimensional image into a one dimensional long stripe, leaving the second dimension for the spectrum. The long stripe exactly matches the entrance slit of a cooled long slit grism spectrometer. The dispersed spectra in the exit of the spectrometer are then collected by a 256×256 HgCdTe NICMOS III detector. The instrument, except for the slicer, is cooled to 77K to suppress the thermal background in the K-band.

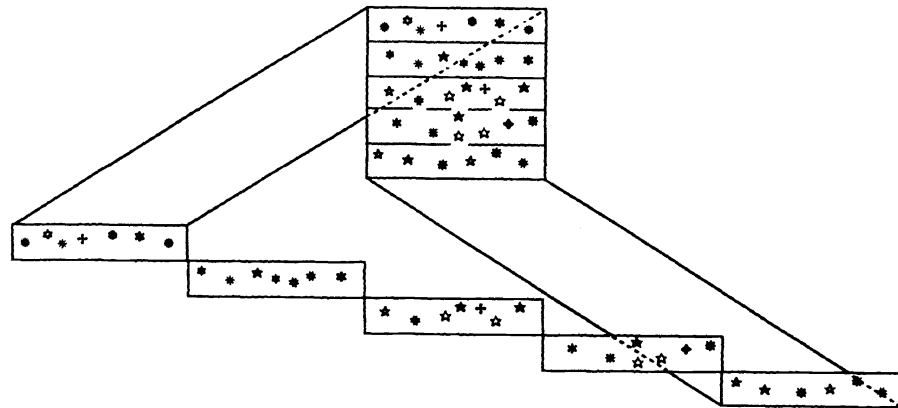
The image slicer accepts a quadratic field in the sky and cuts it into 16 parallel stripes which are then rearranged as illustrated by Fig. 1. At this point the image is still multi chromatic. The fact that the resulting slit is not a straight line but looks stair-like does not affect the performance of the spectroscopy, it only shifts the spectra on the detector by a small amount with respect to each other. Currently the pre-optics in front of the image slicer allow the spatial scale to be set to 0.3" or 0.5"/pixel at a 4 m telescope. This is equivalent to the highest throughput that the instrument can handle without vignetting.

2.2 The image slicer

In this section the optical concept of the image slicer shown in Fig. 2 will be explained in some detail. Mainly three types of image slicers have been applied in optical astronomical instruments so far: The Bowen-Waraven slicer (Richardson, Fletcher & Grundmann 1972), the Richardson slicer (Richardson 1972), and optical fibers (Vanderriest & Lemonnier 1987, Barden & Wade 1988; Arribas, Mediavilla & Rasilla 1991). However none of these type seemed to be applicable within 3D. In the Bowen-Waraven slicer the spatial information is lost after the slicing and the Richardson type is too large and too complicated to adjust.

A slicer using optical fibers seemed to be technically feasible. However, due to the low f/λ number of fibers such a slicer would have to be cold baffled and therefore being operated under more or less cryogenic temperatures in the dewar. Commercially available fibers for the optical waveband could not be used because they tended to change characteristics at 77K due to changes in

Fig. 1. The working principle of the 3D image slicer is demonstrated with an image being sliced in 5 stripes. The real 3D slicer cuts an image into 16 stripes. Top: original image. Bottom: The single slices are optically rearranged in the way shown.



diffraction and dispersion of cladding and core material. Cryogenic fibers exist now but were not commercially available at the time of the design review of 3D three years ago.

As a consequence, a new type of optical slicer was developed for 3D. It only consists of gold coated plain mirrors made of Cerodur and is not temperature sensitive. The slicer (Fig. 2) is composed of two sets of mirrors and a mechanical support structure made of Cerodur as well. The idea behind the design is that the first set of mirrors slices an image into 16 stripes and deflects them into different directions while the second set of mirrors picks up the individual stripes and aligns them into one contiguous long stripe such that the pupils of the 16 single stripes coincide again. Optically, the recombined 16 single stripes are almost indistinguishable from a single long slit and can directly be feed into a conventional cold spectrometer.

The first and smaller stack of mirrors is located at the focal plane of the telescope beam. Each single mirror is about 8 mm long and 0.4 mm high and their normal vector point within 20 arcsec into the calculated directions. The 16 small mirrors and all other

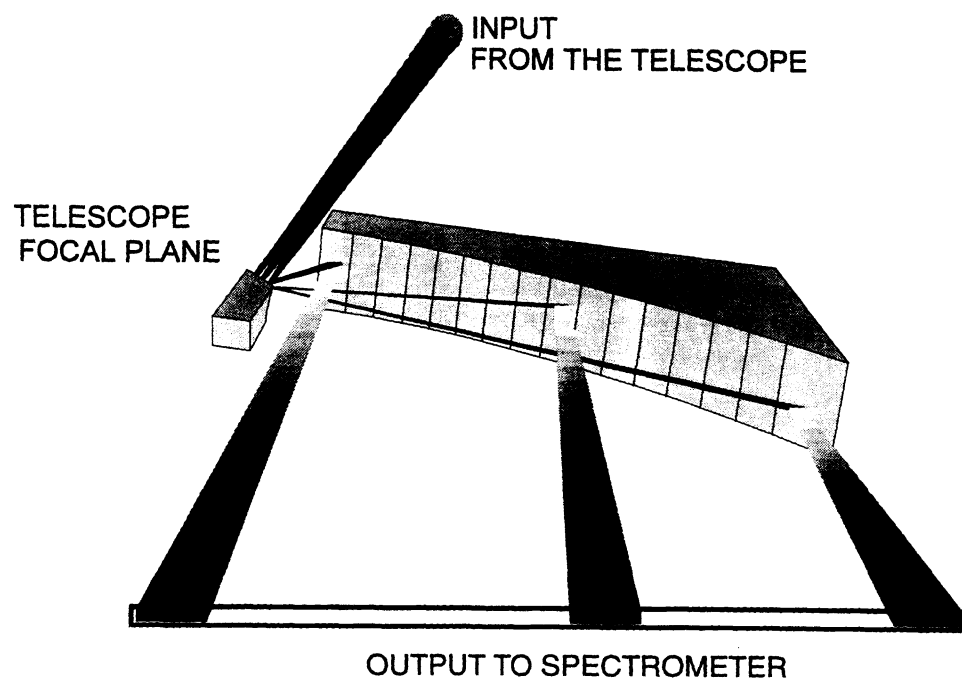
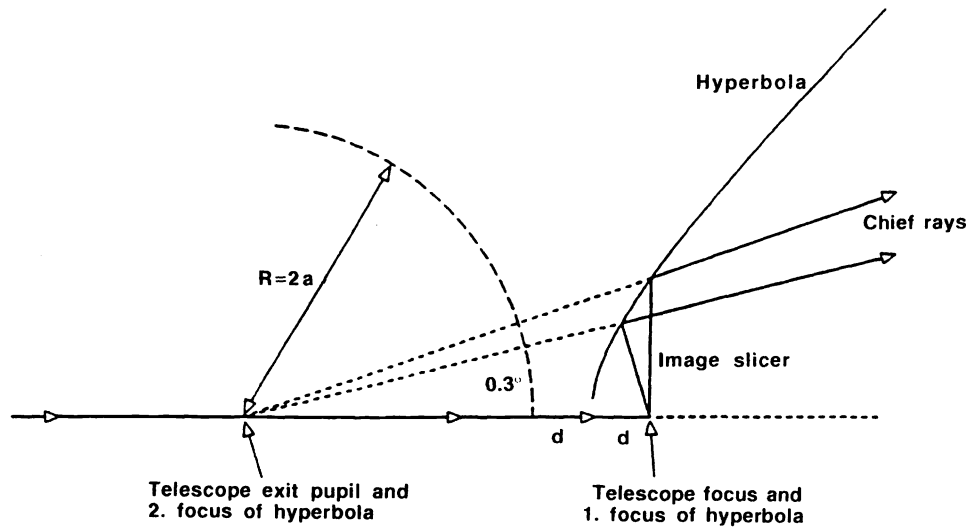


Fig. 2. The image slicer for the 3D spectrometer.

Fig. 3. Design of the 3D image slicer: All chief rays from all individual slices originate from a virtual pupil at the same location as the telescope exit pupil (Weitzel 1994).



parts of the slicer are not glued together but optically contacted by molecular adhesive forces. The second set of mirrors is made as one piece replicated from a master negative. The area centres of these mirrors all lie on a hyperbola such that the two foci of the hyperbola coincide with the telescope focus and the position of the entrance pupil of the unsliced image as illustrated in Fig. 3. The direction of the optical axis after the slicer then slightly differs by 0.3° from the direction of the telescope axis. The image slicer transforms the locations of the single stripes such that the foci of their area centers lie on a circle of radius $2a$ around the second focus of the hyperbola with $2*(a+d)=p$, where d is the distance between the two slicer components and p is the distance between the pupil and the telescope focus. The entrance slit of the spectrometer is therefore virtual.

The overall optical transmission based on geometrical raytracing is 94%, the diffraction at the edges of the small mirrors is negligible.

2.3 The grism

The decision in favor of a grism instead of a reflection grating was based on four arguments: The use of a grism allows a much more compact design, because the lenses can be placed close to the dispersing element; a grism introduces less optical aberrations; the optical adjustment is simpler; the exchange of grisms is straightforward. A grism is usually designed such that the light enters through the flat front surface perpendicular to the beam and exits through the grating area. For a selectable wavelength the beam passes straight through without any deflection so that a grism is preferentially used on-axis which explains the compact optical design.

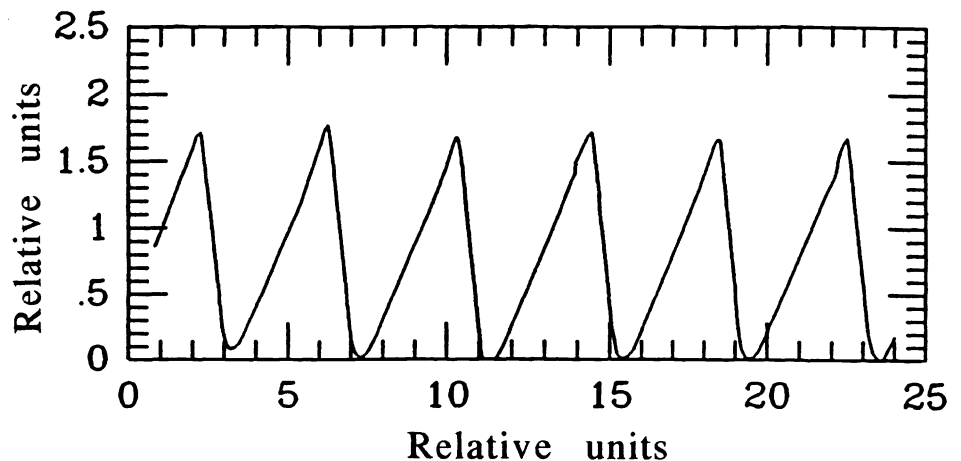


Fig. 4. Measured groove profile of the 3D K-band KRS-5 grism. The grating angle is 24° and the grating constant is $7.68 \mu\text{m}$ (Weitzel 1994).

The critical issue with gratings is the choice of the material. The dispersion of a grism is smaller by a factor of $2/(n-1)$ compared to a reflection grating where n is the refractive index. A high refractive index is therefore desirable because it keeps the prism angle and the mechanical size of the grism small and yields a higher grating efficiency averaged over the free spectral range. If the prism angle grows beyond 30° the simple scalar grism theory is not applicable any more and the full electromagnetic theory is required instead (Neviere 1991; Dekker, D'Odorico & Arsenault 1988). In replicated gratings where the grating is glued to the side of a prism with a resin of refractive index of about 1.6, the refractive index of the prism cannot be made much higher than this number or total internal reflection will occur.

Having investigated all available high refractive materials, we finally selected KRS-5 as the best candidate. KRS-5, a compound of thalliumiodide and thalliumbromide, has a high refractive index of 2.4, excellent transmission, low hardness, and its availability as single crystals. The relative softness of KRS-5 compared to other crystals like ZnSe turned out to be the key element in achieving excellent groove profiles (Fig. 4) and therefore little straylight. Currently three gratings are available for 3D: H-band, K-bandwidth $\lambda/\Delta\lambda=1000$ and short half K-band, $\lambda/\Delta\lambda=2000$. All gratings are coated on the plain front side and have efficiencies of $\geq 60\%$. These are, to our knowledge, the first directly cut NIR gratings of high efficiencies.

2.4 The optical design

The optical design of the cold spectrometer is illustrated in Fig. 5. The collimator and camera are each designed as a 3-lens systems. The first two lenses are mechanically cut to the minimal size in order to save weight and space. The two flats are made from Cerodur. The second flat can be tilted vertically by means of a Queensgate piezo translation stage which slightly shifts the spectrum across the detector in order to fully sample the spectra. A cold shutter blade, driven by a cold stepper motor, sits in front of the camera. The movable stage at the position of the pupil can hold 2 gratings at a time. The stage is motor driven and allows for the exchange of the two gratings on the fly.

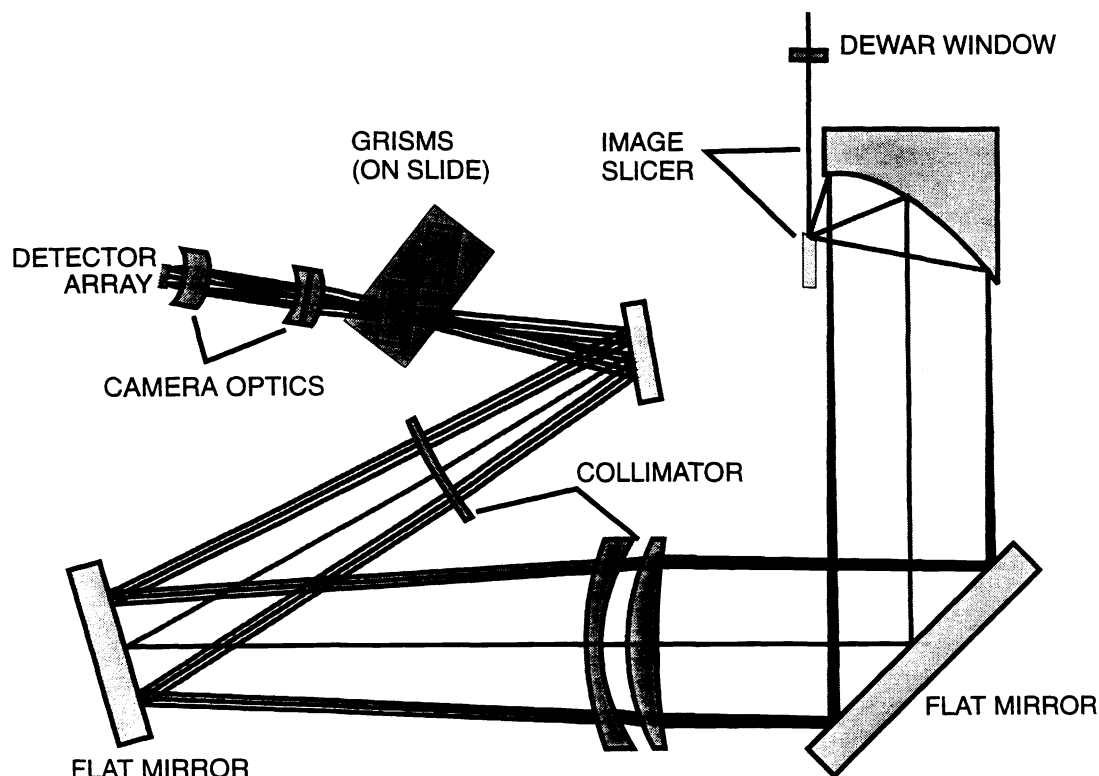


Fig. 5. *Optical design of 3D.*

The optical design was mainly constrained by the fact that the long entrance slit should be imaged onto the detector such that its length exactly matches the 256 pixels of the detector side. Then the width of the slit exactly matches the pixel-to-pixels spacing of 40 μm , thus demanding a demagnification of the entrance slit by a factor of 10. The absolute focal length of the collimator is a compromise between the desire for a compact instrument and the demand that bending of the exit slit should be small enough not to degrade the spectral resolution and to be easily handled by the data reduction software. The optical design was optimized for 77K using a commercial ray tracing program from Kidger-Optics. The image quality of the spectrometer is excellent: For K-band spectroscopy the geometrical blur on every position in the camera focus is smaller than 10 μm . The optical transmission of 3D from the entrance window to the last camera lens including the K-band grism and K-band filter is about 35%.

2.5 Electronics and data acquisition

The detector is electronically divided into four quadrants, each of which is controlled by the standard IR-Labs readout electronics. Among the different available read out schemes only the *correlated double sampling* has been used for the observations because it gave the lowest effective read noise. In this clocking scheme a RESET command followed by two non-destructive READ commands is used. The time gap between the two READs is the integration time which can be selected. Thus two images are read out during a complete sequence. The data of the four detector quadrants are sent via a fiber link to 4 independent digital signal processors (DSPs). DSPs subtract the pre-exposure from the post-exposure image for each quadrant. The control VME computer then receives the data, mosaics it together and stores it on disk.

A careful consideration of the grounding concept in both the analog and digital branch of the IR-Labs electronics led to several modifications with the result that the single read noise of the detector was cut down by a factor of two to 25e-. This increased the instrument sensitivity in the H- and part of the K-band between the OH lines, which are generally detector noise dominated, by an corresponding factor. The read noise will be reduced even further by applying a detector readout scheme called *multiple read* (Fowler & Gatley 1990), which is currently being implemented.

2.6 Atmospheric seeing correction

Rapid Off-Axis GUider Experiment (ROGUE) is a high sensitivity first order seeing corrector which uses a piezo controlled flat mirror in the pupil in order to correct for image motion in real time. It has been developed to improve the spatial resolution of 3D but can be applied to other NIR instruments as well. A full description is given by Thatte et al. (1995) elsewhere in this volume.

3. Data reduction

3.1 Raw data

The 3D data reduction is based on the GIPSY software package (van der Hulst et al. 1992) because it handles data cubes very effectively and provides an user friendly interface to implement dedicated additional software written by the applicant.

A typical H-band raw data frame is shown in Fig. 6. It more or less resembles an output from a long slit spectrometer. The vertical axis represents the wavelength from short to long while the horizontal axis is along the slit. It consists of 16 single adjacent slits which are slightly shifted in wavelength with respect to each other. This reflects the fact that the single slits are not fully aligned in the entrance of the spectrometer but only touch each other at one corner (see section 2.2 and Fig.1). Fig.6 is mostly dominated by thermal background, atmospheric OH emission lines and a bit of straylight. These contaminations together with the dark current of the detector are removed by subtracting a blank sky image taken near the object with the same integration time. The result of the subtraction for a K-band image is shown in Fig. 7, which reveals the existence of the continuum emission from an object (a galaxy) in the data as well as several of emission lines. Information about the morphology of the object however cannot yet be easily discerned at this stage of the data reduction.

3.2 Flatfielding and Calibration

Before the two dimensional image can be converted into a three dimensional data cube, it must be flatfielded and wavelength calibrated.

The unique nature of 3D implies that the source used for flat fielding must be both spatially and spectrally flat. As no source satisfies both these constraints simultaneously, the flat field is created from two separate images, one contributing the spatial flat

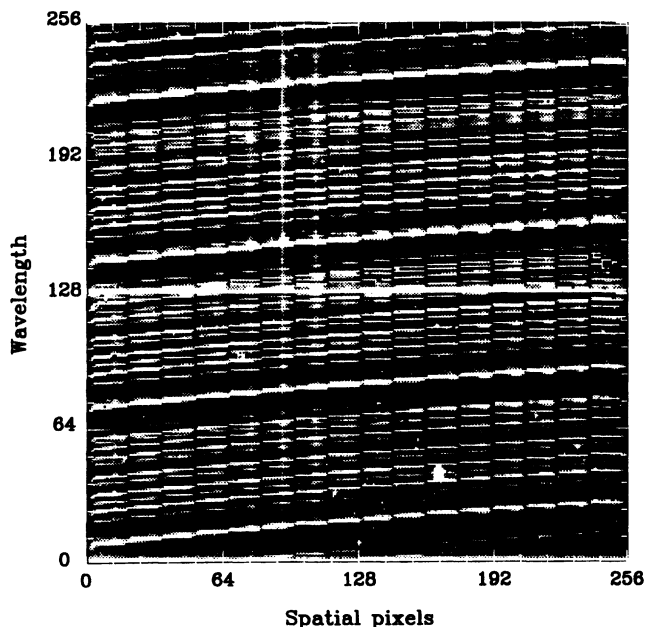


Fig. 6. Raw 3D H-band data frame. The 16 single slits are clearly visible. The vertical structure is continuum emission from an extended object, the white spot is a cluster of bad pixels.

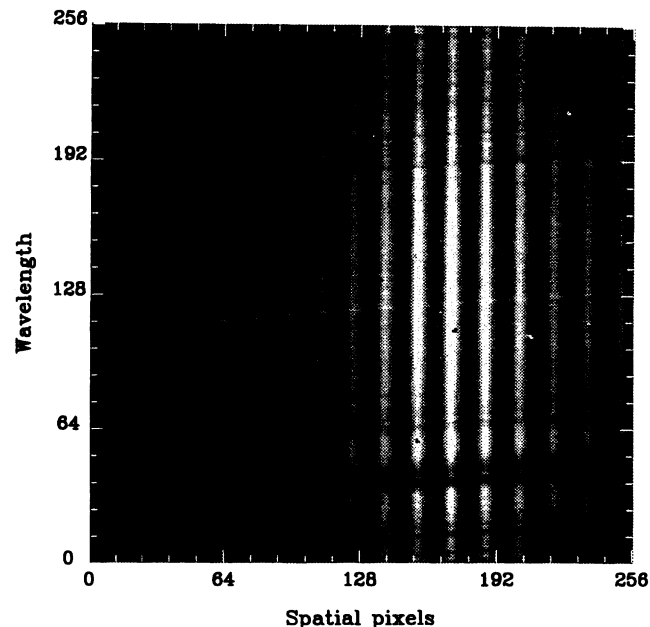


Fig. 7. Sky subtracted 3D K-band data frame. The object is an extended galaxy showing some emission lines. The absorption lines are of telluric origin.

field the other one contributing the spectral flat field. Usually the spatial flat field is obtained from a differential image of the dome (light on/off). Collapsing each of the spectra within the same wavelength interval results in one line of pixels representing the broad-band flux of the dome. As the spectral characteristics are the same in all 256 spectra, the pixel to pixel variations along the line should only be attributable to irregularities in slicer efficiency and the detector response.

The spectral flat field is obtained in a similar manner. The template source is a glowing Nernst rod whose spectrum roughly approximates that of a blackbody and does not contain emission or absorption lines. If the temperature is selected properly, the spectrum is almost flat within the wavelength band. If a differential image (glower on/off) is normalised to the same intensity at a given wavelength, differences between the 256 spectra are then only attributable to irregularities in the detector response. The overall flat field is thus created by multiplying every row of the normalised spectral flatfield with the collapsed spatial flatfield and normalising the result image.

It should be noted that an accurate knowledge of the spectral shape of the Nernst-glower is not critical to the data reduction process. In most cases, the observed spectrum of the source under study is divided by the spectrum of a template star, in order to remove any spectral features introduced by the atmosphere. If both sets of data, the template star as well as the object, have been processed with the same flat field, the Nernst-glower spectrum will finally be divided out of the data.

Each of the 256 spectra has to be wavelength calibrated individually in two steps: The wavelength of each pixel has to be determined and the spectra have to be redistributed on a regular wavelength grid identical for all spectra. The first step is performed by comparing the measured emission lines of a spectral calibration source (e.g. neon lamp for K-band, telluric OH lines in H-band) with the theoretical spectrum. The spectral redistribution is then achieved by interpolating the data in each column of the original image by means of polynomial interpolation. The grid spacing is 2 nm, the mean value in all 256 spectra. The fact that the original spectra are shifted against each other explains that the wavelength calibrated image contains 300 instead of 256 pixels in the direction of the wavelength. In the calibrated image extended emission and absorption lines form horizontal lines across (part of) the image. Therefore row number (counted from bottom) and wavelength are convertible. In a calibrated K-band data set the transformation is: $\lambda [\mu\text{m}] = \text{row}/500 + 1.85$.

3.3 Datacube and bad pixel correction

Each image slice is designed to span exactly 16 detector pixels, 16 such slices constituting the complete sky image. Practical limitations and fabrication of the optical elements as well as imperfect knowledge of cold refractive indices lead to a total image extend of 252.8 pixels, instead of the theoretical 256 pixels. Small errors in the optical adjustment of the individual image slicer mirrors can also introduce variations in the number of detector pixels spanned by each image slice.

In order to reconstruct the two dimensional image from the 16 image slices, it is necessary to determine the relative shift between the center points of the slices. An exposure is made while moving a star across the entire FOV in a north-south direction. The image slices are then aligned so as to yield a stellar image smeared precisely in a vertical direction, allowing us to determine the relative shift of each slice to a fraction of a pixel. The amount of shift is non-integer, making it necessary to re-sample the data from each spatial slice. The re-sampling is carried out either by interpolating or using FFT techniques, since unlike the spectral dimension, the spatial data is adequately sampled. The edge of each slice often contain pixels receiving light from two spatial slices. These pixels do not contain any useful information, and are discarded.

Permanent bad pixels are included in a bad pixel list. Transient unusable pixels due to cosmic ray hits or overexposure are detected by an algorithm and marked in an individual bad pixel mask frame that is associated with every data frame. If necessary, the bad pixels can be interpolated in the datacube using a 3 dimensional interpolation routine. The routine includes criteria about the conditions for a successful interpolation and interpolates bad pixels which match these criteria.

4. Astronomical results

4.1 Introduction

Many of the exciting open question of current observational astronomy deal with the exploration of subarcsec structures in both galactic and extragalactic sources. Adressable issues include

- How can Seyfert 1 and 2 nuclei be understood in terms of a unified scheme, how do the molecular clouds interact with the NLR, what is the central mass, the nuclear stellar population and dynamics like?
- What is the history of starbursts phenomena and how do they proceed from one location to the next, what role does the molecular bar play that is often observed in the nuclear region, what is the current stellar population and does a connection to Seyfert activity in the nuclei exist?
- How does the stellar population in the very nucleus of our galaxy look like and does the center of our galaxy harbour a black hole?
- Are some of the bright high z galaxies that are currently being found primeval galaxies or gravitational lenses?
- What is the evolutionary state of star formation in high z ($z \geq 2$) radio galaxies and ho was it induced?

These and more issues are most effectively tackled with an instrument like 3D. In this chapter we present a selection from recent results which addresses some of the topics mentioned above.

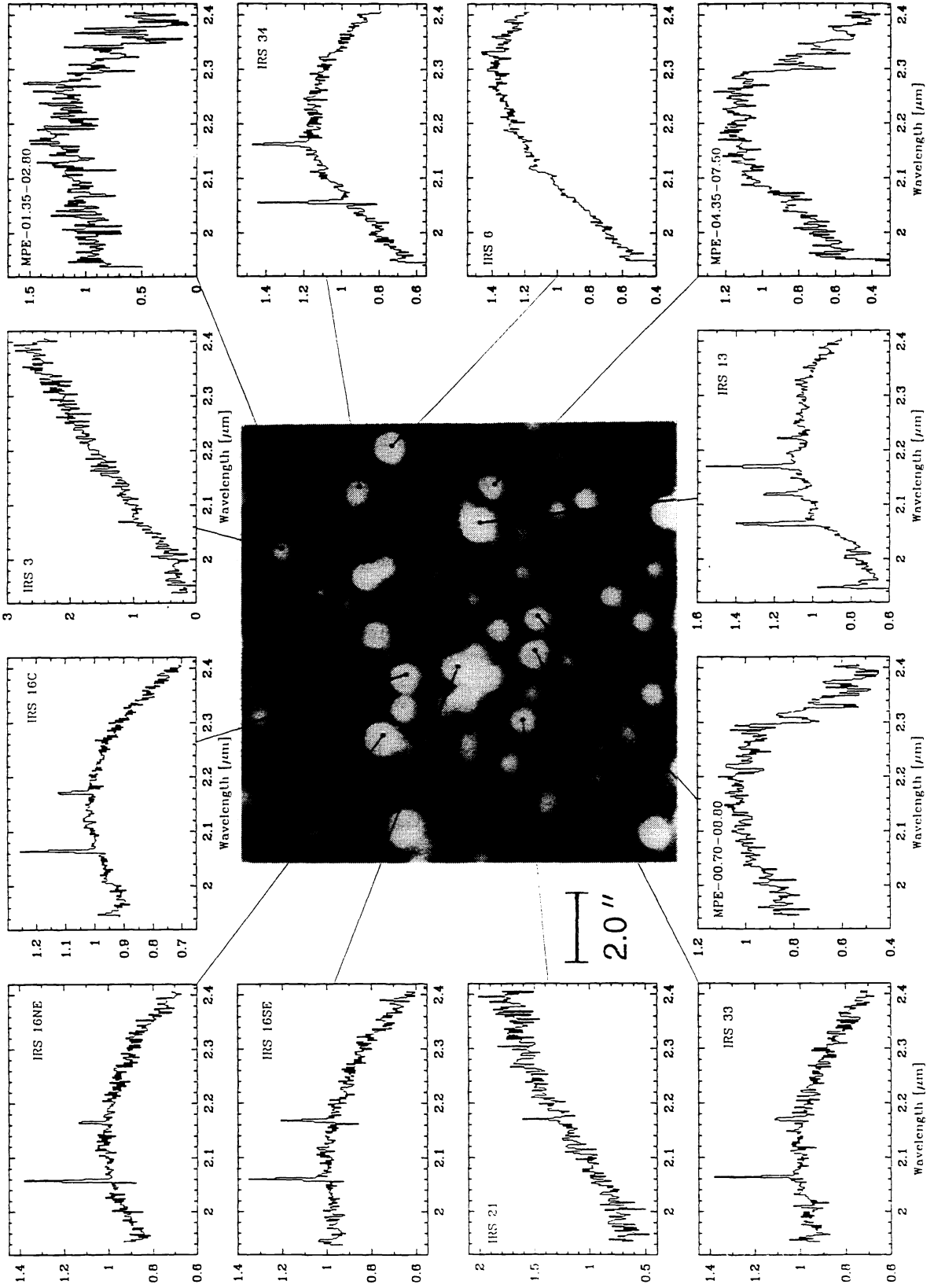
4.2 The central stellar cluster of our galaxy

There is an ongoing debate on the nature of the central source in our galaxy and the source of the luminosity in the central parsec (Genzel, Hollenbach & Townes 1994). 3D observations at the 2.2m ESO telescope of the central 10 arcsec now for the first time delivered complete K-band spectra ($\lambda/\Delta\lambda=1000$) of about 25 stars (Krabbe et al. 95). A preliminary extract, shown in Fig. 8 (overleaf), displays a K-band image of the galactic center (Eckart et al. 1995) convolved to 0.4" spatial resolution together with 12 stellar spectra obtained with 3D. The quality of these spectra is high enough, even if their apparent separation is sometimes smaller than 1 arcsec, that all 25 stars could be classified and placed within an HR-diagram and stellar population synthesis models could be applied. The most likely scenario of the formation of the massive stars now is a small starburst between 4 and 8×10^6 years ago. Some recently formed, and therefore still highly obscured, massive stars may have been transported into the central core along with orbiting gas streamers.

In addition to the classification of the stellar spectra we cross-correlated the spectra and determined the velocity dispersion of the cluster stars. Including earlier data of some stars further out, the radial velocity dispersion of 35 early and late type stars with dis-

Galactic Center: K-Band Spectra of Central Cluster Stars

3D



tances of 1" to 12" from the dynamical center (SgrA*) is 159 ± 19 km/s. This result strongly favours the existence of a central dark mass of $\sim 3 \times 10^6 M_{\odot}$ within ~ 0.14 pc of the dynamic center.

4.3 IC 342

IC 342 a classical starburst galaxies and is well suited for a detailed investigation due to its small distance of 1.8 Mpc, its almost face-on orientation and its much lower internal extinction compared to, for example, M82. In its central region IC 342 shows many typical signs of ongoing star bursts which made it a target for many investigations specially in the sub-mm and radio regime. IC 342 shows a molecular bar in ^{12}CO , ^{13}CO , and HCN, which peaks at the NIR- and continuum center and extends in the north-south direction for about 1'. The central region in the molecular line emission forms a ring like structure with a diameter of about 6".

3D data have been obtained at the 3.5m telescope on Calar Alto at 4 spatial positions on IC 342 covering much of the central 12" and revealing a wealth of information. Fig. 9 displaying the K-band spectra at different positions on and in the vicinity of IC 342s nucleus shows clearly how the physical conditions vary in and along the starburst ring. A continuum subtracted channel map at the position of the Br γ emission line, shown in Fig. 9 in contours, traces very nicely the morphology of the starburst ring and demonstrates how the data cube can be investigated in detail.

4.4 IRAS F10214+4724

At a redshift of 2.286 the galaxy IRAS F10214+4724 (hereafter F10214) is suggested to be one of the most luminous single objects in the universe. A bolometric luminosity of $L_{\text{bol}} \sim 1.4 \times 10^{14} L_{\odot}$ (Rowan-Robinson et al. 1991) and a large mass of molecular gas ($\sim 2 \times 10^{11} M_{\odot}$ Solomon, Radford & Downes 1992) has led to speculation that this source even represents a true primeval galaxy in the process of forming the bulk of its stellar population and enriching its ISM with metals for the first time. However, the distorted appearance of F10214 in high resolution K-band images from the Keck telescope, the presence of companions, and statistical arguments makes it plausible that gravitational lensing may be involved (Matthews et al. 1994, Elston et al. 1994) . Thus the nature and evolutionary state of this galaxy remains unclear. The field nearby F10214 contains a number of fainter galaxies. The redshifts of these galaxies are unknown and it is unclear whether F10214 is a member of this cluster or whether one of them could serve as a foreground galaxy in a possible gravitational lens.

Fig. 10 shows a preliminary K-band spectrum which results from 10000 secs of integration on this object, obtained at the 3.5m telescope on Calar Alto (Spain). The spectrum is the best that exists so far (compare to Elston et al. 1994) and not only clearly separates H α and one NII line but for the first time shows the two SII lines. The continuum map (sum of the continuum channels only) shows two other accompanying galaxies which do appear in the K $_S$ -band map of Matthews et al (1994) as well. The morphology of the H α emission line looks different from the morphology of the corresponding continuum source and might even be different from the NII emission as well. H α is clearly extended east-west compared to the continuum, suggesting that the interpretation of F10214 being a simple gravitational lens maybe less likely. The K-band spectrum of the other two galaxies do not show any strong emission line is the entire K-band. This means that either these galaxies are located at a different redshift or if they belong to the same cluster as F10214 only the latter is experiencing an starburst that gives rise to such a tremendous luminosity.

5. References

- Arribas S., Mediavilla E. & Rasilla J.L., 1991, ApJ., **369**, 260
Barden S.C. & Wade R.A., 1988, in *Fiber Optics in Astronomy*, ASP Conference Series Vol. 3, ed. S.C. Barden
Blietz, M., Cameron, M., Drapatz, S., Genzel, R., Krabbe, A., van der Werf, P., Sternberg, A. & Ward, M.J., 1994, ApJ.Lett., **421**, 92
Decker H., D'Odorico S. & Arsenault R., 1988, A. & A., **189**, 353
Eckart A., Genzel R., Hofmann R., Sams B.J., Tacconi-Garman L.E., 1995, ApJ., in press
Elston R., McCarthy P.J., Eisenhardt, P. Dickinson M., Spinrad H., Januzzi B.T., Maloney P., 1994, A.J., **107**, 910
Fowler A.M. & Gatley I., 1990, ApJ.Lett., **353**, L33
Genzel R., Hollenbach D.J., Townes C.H., 1994, Rep. Prog. Phys., **57**, 417
Krabbe A., Genzel R., Drapatz S., Rotaciuc V., 1991, Ap.J. Lett., **382**, L19

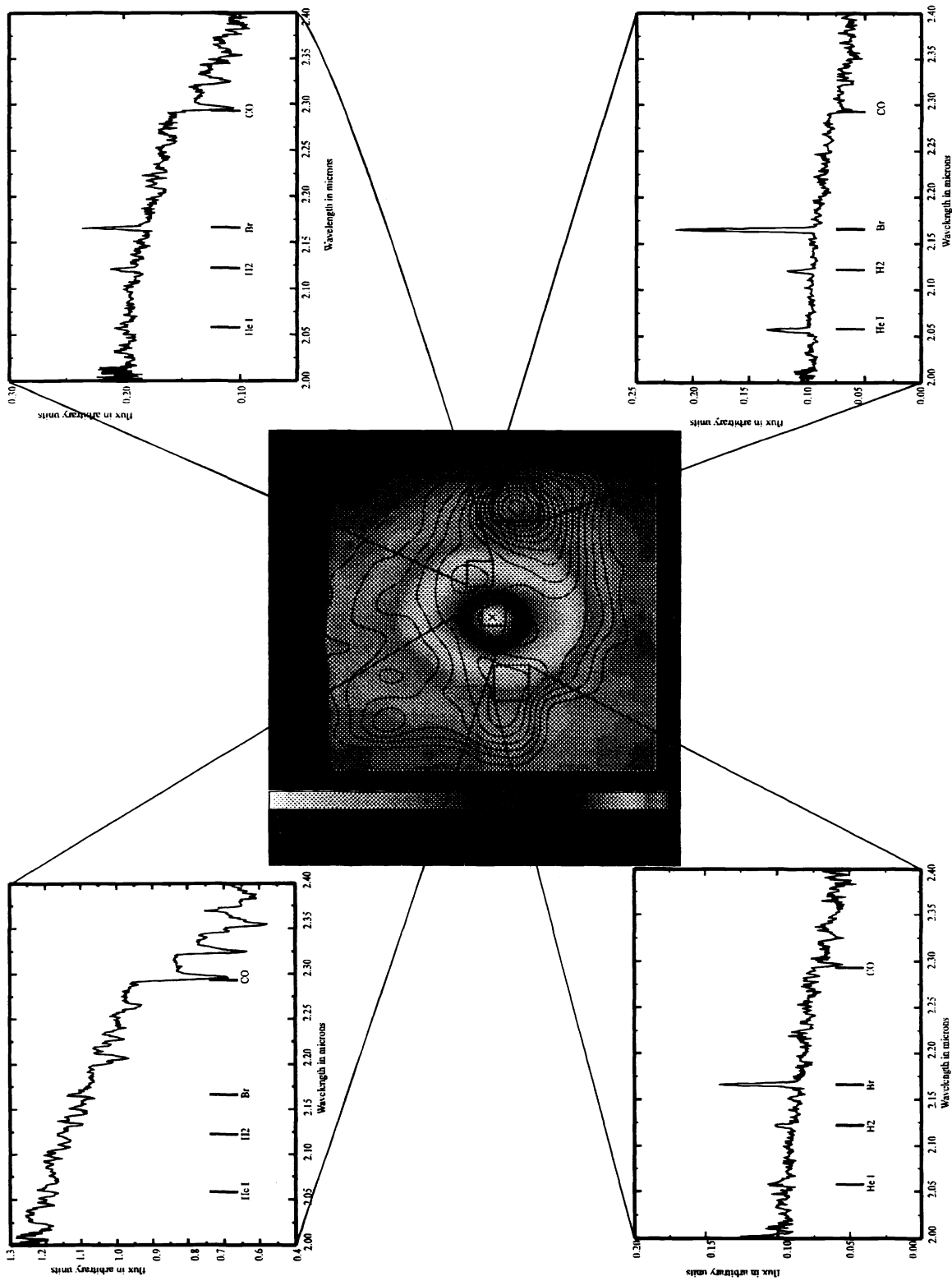


Fig. 9. Spectra of various regions in the central 100 pc of IC 342. The gray scale image represents the continuum, the Br γ (2.16 μ m) line emission is overlaid in contours.

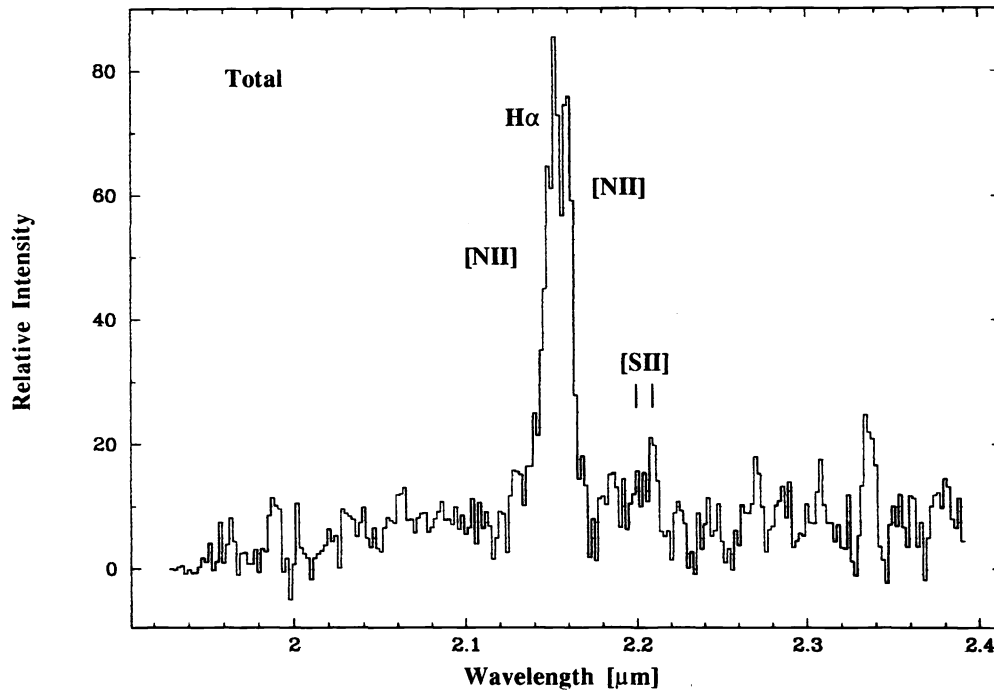


Fig. 10. *K*-band spectrum of F10214+4724 at a redshift of 2.283.

- Krabbe A., Rotaciuc V., Storey J.W.V., Cameron M., Blietz M., Drapatz S., Hofmann R., Sämann G. & Genzel R., 1993, P.A.S.P., **105**, 1472
- Krabbe A., Genzel R., Echart A., Najarro F., Lutz D., Cameron M., Kroker H., Tacconi-Garman L.E., Thatte N., Weitzel L., Drapatz S., Geballe T., Sternberg & Kudritzki R., 1995, Ap.J., submitted
- Lutz, D., Krabbe, A., Genzel, R., 1993, Ap.J., **418**, 244
- Neviere M., 1991, Appl. Optics, **30**, 4540
- Matthews K., et al., 1994, Ap.J.Lett., 420, L13
- Richardson E.H., 1972, in *Auxiliary Instrumentation For Large Telescopes*, ESO/CERN Conf. proc., eds. S. Lausten & A. Reiz
- Richardson E.H., Fletcher J.M. & Grundmann W.A., 1972, in *Very Large Telescopes, their Instrumentations and Programs*, proc. of the IAU Colloquium No. 79
- Rowan -Robinson M., et al. 1991, Nature, **351**, 719
- Solomon P.M., Radford S.J.E. & Downes D., 1992, Ap.J.Lett., 398, L29
- Thatte N. et al. 1995, this volume
- van der Hulst J.M., Terlouw J.P., Begeman K., Zwitser W. & Roelfsema P.R., 1992, *The Groningen Image Processing System, GIPSY*, in: *Astronomical Data Analysis Software and Systems I*, eds. D.M. Worall, C. Biemesderfer & J. Barnes, ASP Conference Series No. 25, p.131
- Vanderriest C. & Lemonnier J.P., 1987, in *Instrumentation for Ground-Based Optical Astronomy 1987*, 9th Santa Cruz Summer Workshop, ed. L.B. Robinson
- Weitzel L., 1994, Ph. D. Thesis, Ludwig-Maximilian-Universität München